

Measurement of the atom-surface van der Waals interaction by transmission spectroscopy in a wedged nanocell

T. Peyrot, N. Šibalić, Y. R. P. Sortais, and A. Browaeys

Laboratoire Charles Fabry, Institut d'Optique Graduate School, CNRS, Université Paris-Saclay, F-91127 Palaiseau Cedex, France

A. Sargsyan and D. Sarkisyan

Institute for Physical Research, National Academy of Sciences - Ashtarak 2, 0203, Armenia

I. G. Hughes and C. S. Adams

Department of Physics, Rochester Building, Durham University, South Road, Durham DH1 3LE, United Kingdom



(Received 7 May 2019; published 1 August 2019)

We demonstrate a method for measuring atom-surface interactions using transmission spectroscopy of thermal vapors confined in a wedged nanocell. The wedged shape of the cell allows complementary measurements of both the bulk atomic vapor and atoms close to surfaces experiencing strong van der Waals atom-surface interaction. These are used to tightly constrain the dipole-dipole collisional parameters of a theoretical model for transmission spectra that accounts for atom-surface interactions, cavity effects, collisions with the surface of the cell, and atomic motion. We illustrate this method on a cesium vapor in a sapphire cell, demonstrating that even the weakest of the van der Waals atom-surface interaction coefficients—for ground-state alkali atom transitions—can be determined with a very good precision. This result paves the way towards a precise quantitative characterization of atom-surface interactions in a wide range of atom-based nanodevices.

DOI: [10.1103/PhysRevA.100.022503](https://doi.org/10.1103/PhysRevA.100.022503)

I. INTRODUCTION

Atoms close to surfaces offer new possibilities for engineered atom-atom and atom-light interactions through light confinement and surface-mode excitations [1–4], ultimately down to the single-photon level [5–7]. This has stimulated a recent growth in the number of platforms where atoms are kept close to surfaces, ranging from nanofibers [4,8–12] and nanocells [13,14] to waveguides [15] and microtoroidal optical resonators [6]. Simultaneously, shrinking the dimensions of atom-based sensors [16–18] increases the number of atoms close to a surface relative to atoms in the bulk. Atom-surface interactions are therefore becoming increasingly important: they may limit the ultimate achievable precision of atom vapor sensors and they are crucial in understanding the dynamics in each new platform [6,11,12]. However, despite their significance, direct measurements of atom-surface interactions are scarce.

Measuring the van der Waals (vdW) atom-surface interaction—that scales with the distance z to the surface as $1/z^3$ [19]—is challenging as it requires placing the atoms in a given internal state at a distance $z < \lambda/(2\pi)$ from the surface [20]. Here, λ is the wavelength of the strongest atomic transition from the considered state. Previous experiments on vdW atom-surface interactions used sophisticated techniques such as reflections of cold atoms on a surface [21–24], high-lying atomic states [25], or both [26]. High-lying states allow easier access to the vdW regime as: (i) transitions among higher-lying states correspond to longer wavelengths λ , relaxing the constraint on the atom-surface distance; and (ii) these transitions have larger dipole matrix elements,

resulting in a stronger vdW coefficient C_3 in the atom-surface potential, $V(z) = -C_3/z^3$. However, for many applications [2–6,11–15], it is the properties of the ground-state atom-surface potential that are of most interest.

Spectroscopy of thermal vapors contained in cells [25, 27–29] is an attractive method for the measurement of atom-surface interactions since it can be used for a large range of vapors, atomic or molecular, and surfaces. However, measurements have low precision for weak vdW interaction strengths of ground-state atoms, mainly limited by the uncertainty in estimating collisional processes in dense vapors [25,27]. A recent method that measured the ground-state vdW interaction based on *fluorescence* spectroscopy in low-density thermal vapors [30] raised debate [31] about the absolute achievable precision of the measurements since the theoretical model used [30] neglected atomic motion in the spatially varying atom-surface potential. Finding simple and precise methods that would allow reliable extraction of the ground-state atom-surface potential parameters, and characterization of the atom dynamics in the proximity of surfaces in new platforms, remains an open goal.

Here, we demonstrate an alternative method for measuring the atom-surface interaction. Using a wedged nanocell, we obtain *transmission* spectra for a vapor thicknesses range of $L = 50\text{--}275$ nm. This allows access both to the region where vdW interactions have strong effects on the total transmission signal and the region where atoms in the bulk, not affected by the vdW-induced shifts, dominantly contribute. Spectra from the thick region yield the collisional parameters for the bulk atomic vapor, thus allowing reliable fitting of thin-region spectra using our model. The model includes atomic motion

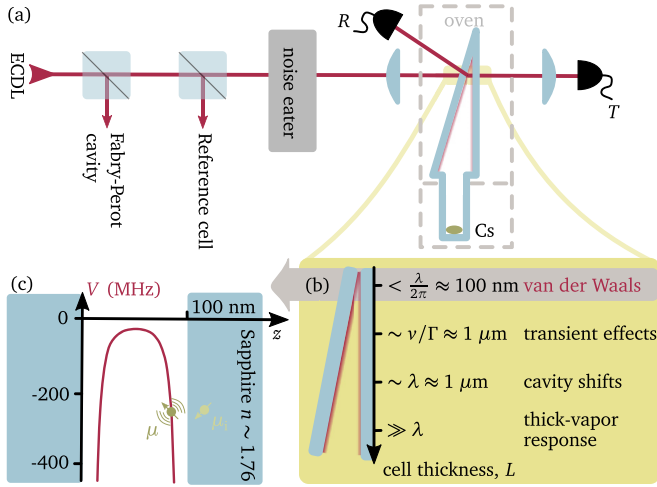


FIG. 1. (a) A frequency-calibrated, intensity-stabilized external cavity diode laser (ECDL) probes a cesium vapor confined in a wedged sapphire nanocell. The cell thickness is locally measured using interference in the reflection signal R . (b) The wedged shape of the cell allows probing the transmission T in thick cell regions, where the contribution of atoms close to the surfaces is negligible compared to the contribution of the atoms in the bulk. It also allows going to the sub-100-nm-thick region where the atoms are strongly affected by the van der Waals potential due to the interaction of their dipole μ with its image μ_i in the surface (c). This gives rise to a position z -dependent level shift $V(z)$, here calculated for the $D1$ Cs transition.

in a spatially varying atom-surface potential, in addition to other surface-induced transient effects [32]. This procedure allows measurement of the atom-surface potential even for the ground-state transitions with a good precision. We illustrate it by a measurement of the vdW-induced shift of the cesium $6S_{1/2} \rightarrow 6P_{1/2}$ transition in the presence of a sapphire surface. Our model significantly improves on a phenomenological one based on a fitted line shift and broadening parameters, and shows excellent agreement with the measured spectra.

II. EXPERIMENTAL SETUP

The experimental setup [32] is presented in Fig. 1(a). We use an external cavity diode laser (ECDL) to probe the D_1 ($\lambda = 894$ nm) transition of a cesium vapor contained in an ultrathin wedged sapphire cell, with thickness varying from $L = 30$ nm to $2\ \mu\text{m}$. We measure the *in situ* vapor thickness L using interference resulting from the far off-resonant reflections from the wedge. With a beam waist of $50\ \mu\text{m}$ ($1/e^2$ intensity), the uncertainty in the determination of L is 5 nm. The frequency scan of the ECDL is linearized using a Fabry-Perot cavity and referenced to a standard 7 cm cesium spectroscopic cell. The laser intensity is stabilized during the scan by an acousto-optic modulator-based noise eater. The wedged nanocell is placed in a double oven: the bottom part containing the cesium reservoir is kept at $235\ ^\circ\text{C}$, and sets the atom number density \mathcal{N} ; the top part with the wedged sapphire windows is kept at a temperature $30\ ^\circ\text{C}$ higher to avoid vapor condensation. The oven is temperature stabilized to $\sim 5\ ^\circ\text{C}$. A low-noise photodiode is used to obtain the transmission signal T subtracted from the background noise.

The theoretical analysis of transmission spectra in nanocells is significantly more complicated than for transmission through bulk vapor [33]. With the reduction of the vapor thickness L , a number of effects starts to play a role [Fig. 1(b)]: (i) for micrometer-thick layers, the cell walls act as a low-finesse cavity, resulting in level shifts [34]; (ii) the cell windows also cause dephasing of atoms upon direct collisions [35]. Atoms flying off the walls experience transient dynamics during a time $1/\Gamma$, with Γ the collisionally broadened linewidth. For a cell thickness below v/Γ (v is the average atom velocity), a significant number of probed atoms experience the transient regime, which significantly modifies the measured transmission [32]. For cesium atoms at a temperature of $\sim 200\ ^\circ\text{C}$, this corresponds to a distance of $\sim 1\ \mu\text{m}$. Finally, (iii) at atom-surface distances $z < \lambda/(2\pi)$, atomic energy levels experience a vdW shift, $V = -C_3/z^3$ [Fig. 1(c)]. This atom-surface interaction comes from the coupling between an atomic dipole and its image dipole in the sapphire surface [36]. To extract this vdW interaction at small atom-surface distances (iii), it is necessary to first account for the effects (i) and (ii) that modify the atom dynamics in thin cells even outside the range of the atom-surface potential.

III. DETERMINATION OF BULK VAPOUR PROPERTIES

We have recently developed a model for the atom response in the bulk [32], away from the influence of the vdW potential, following Refs. [37,38]. To account for the transient atoms dynamics (ii) described above, we solve the optical Bloch equations (Appendix A) for the atom coherence field, $\rho_{21}(z, v, \omega) = \rho_+(z, v, \omega)e^{ikz} + \rho_-(z, v, \omega)e^{-ikz}$, for each atomic velocity v class, where $k = 2\pi/\lambda = \omega/c$ is the laser-field wave vector *in vacuum*. Assuming a loss of coherence in atom-wall collisions [35], one obtains

$$\rho_{\pm}(z, v > 0) = i \frac{d_{FF'} E_{\pm}}{2\hbar v} \int_0^z \exp\left[\frac{\Lambda_{\pm}(z') - \Lambda_{\pm}(z)}{v}\right] dz', \quad (1)$$

$$\rho_{\pm}(z, v < 0) = -i \frac{d_{FF'} E_{\pm}}{2\hbar v} \int_z^L \exp\left[\frac{\Lambda_{\pm}(z') - \Lambda_{\pm}(z)}{v}\right] dz', \quad (2)$$

where E_{\pm} are the co- and counterpropagating driving fields along the z direction, and $d_{FF'}$ is the dipole moment for the hyperfine transition $F \rightarrow F'$. In a bulk cell, away from the range of the atom-surface potential, a level shift Δ_P and a broadening Γ_P of the transition arise due to the atom-atom collisional interaction. Thus, for $z > \lambda/(2\pi)$, Λ_{\pm} in Eqs. (1) and (2) is

$$\Lambda_{\pm}^{\text{bulk}}(z) = [(\Gamma_P + \Gamma_0)/2 - i(\Delta_{FF'} \mp kv)]z, \quad (3)$$

for a laser detuning $\Delta_{FF'} = \omega - \omega_{FF'} - \Delta_P$ from the transition at frequency $\omega_{FF'}$ with radiative linewidth $\Gamma_0/(2\pi) \approx 4.6$ MHz for the Cs D_1 line. Equations (1) and (2) can then be analytically solved, and the polarization of the medium, $P(z, \omega) = \sum_{F,F'} \int_{-\infty}^{\infty} dv 2\mathcal{N}M_b(v)d_{FF'}\rho(z, v, \omega)$, is obtained by summing the contributions from all velocity classes in the Maxwell-Boltzman distribution $M_b(v)$.

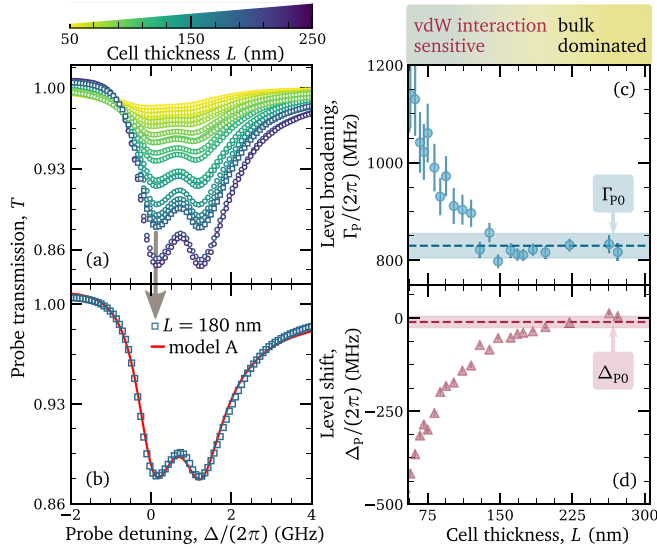


FIG. 2. Determination of the collisional broadening Γ_{P0} and shift Δ_{P0} in the bulk vapor. (a) Measured transmission spectra at 235 °C, for cell thickness L in range 50–225 nm. The left and right peaks correspond to the $F = 4 \rightarrow 3$ and $F = 4 \rightarrow 4$ transitions of the Cs $D1$ line, respectively. Model A, not including atom-surface interactions, fits well with the spectra in (b) the thick part of the cell, allowing the extraction of bulk properties of the vapor from (c),(d) values obtained for large L . For small L , the influence of the atom-surface interactions appears as an additional thickness-dependent line broadening and transition shift.

In order to include the cavity effects (i), we take into account the transmission $t_1 = 2n/(1+n)$ and reflection $r_2 = (1-n)/(1+n)$ coefficients of the driving field E_0 at the two sapphire cell walls (refractive index n). Assuming an optically dilute atomic medium, we neglect the contribution of atoms to the driving field E_{\pm} inside the cavity, so that $E_+ e^{ikz} + E_- e^{-ikz} \simeq t_1/[1 - r_2^2 \exp(2ikL)]E_0\{\exp[ikz] + r_2 \exp[ik(2L - z)]\}$. Similarly, the radiated atomic fields E_{A+} and E_{A-} initially co- or counterpropagating along the z axis, respectively (Appendix A), can be reflected multiple times inside the cavity [32]. They give rise to an atom-induced field outside the cavity,

$$E_{A\pm}(z) = \frac{t_2}{1 - r_2^2 e^{2ikL}} \frac{ik}{2\epsilon_0} \int_0^L dz' P(z', \omega) \exp[\pm ik(z - z')], \quad (4)$$

in the direction of initial emission, and fields $r_2 \exp[2ik(L - z)]E_{A+}$ and $r_2 \exp(2ikz)E_{A-}$, respectively, in the opposite direction, where $t_2 = 2/(1+n)$. Finally, we obtain the transmission factor through the thin-cell system $T = |E_T/E_{0+}|^2$, where $E_T = E_{0+} + E_{A+} + r_2 \exp(2ikz)E_{A-}$ is a superposition of the transmitted atom-induced field and transmitted driving field $E_{0+} = t_1 t_2/[1 - r_2^2 \exp(2ikL)]E_0 \exp(ikz)$.

The model described above (from now on, Model A) fits well to the measured transmission spectra [Fig. 2(a)] for cell thicknesses $L \geq 150$ nm [see, for example, Fig. 2(b)], where the signal is dominated by atoms far from the surface. In this region, fitting the temperature, level shift Δ_P , and broadening Γ_P allows us to obtain the collisional self-broadening $\Gamma_{P0}/(2\pi) = 830 \pm 10$ MHz [Fig. 2(c)] and line

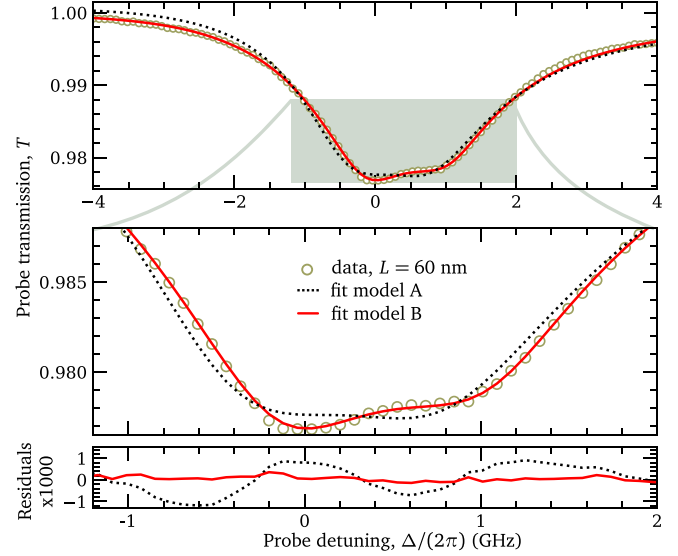


FIG. 3. Comparison of Model B that accounts for vdW interactions with phenomenological Model A. Model A (dotted line), not including atom-surface interactions, misses line-shape features for spectra in the thin-cell region (circles), as highlighted on the zoomed inset. This is despite the fact that in addition to temperature, we take the broadening Γ_P and shift Δ_P as free parameters to phenomenologically account for atom-surface interactions. Model B (solid line)—that includes atom motion in the spatially dependent van der Waals potential explicitly—reproduces the asymmetric double-peak feature perfectly, with only the temperature and C_3 as free parameters when imposing bulk-determined line shift $\Delta_P = \Delta_{P0}$ and broadening $\Gamma_P = \Gamma_{P0}$.

shift $\Delta_{P0}/(2\pi) = -10 \pm 20$ MHz [Fig. 2(d)] in the bulk vapor, arising solely from atom-atom collisions. The value and error bar are the mean and standard error of the fitted values for cell thicknesses $L \geq 175$ nm. The measured broadening is in good agreement with theoretical predictions [39] at 235 °C.

IV. DETERMINATION OF ATOM-SURFACE PROPERTIES

For cell thicknesses $L \lesssim 150$ nm, the contribution from atoms close to the surface becomes significant. The vdW interaction [Fig. 1(c)] offsets the $6S_{1/2}$ and $6P_{1/2}$ levels by different amounts due to the different vdW C_3 coefficients for the two states. Model A captures this atom-surface interaction phenomenologically as a cell-thickness-dependent shift and broadening, as shown in Figs. 2(c) and 2(d). However, this phenomenological fit does not provide direct access to the C_3 vdW coefficient. In addition, Fig. 3 indicates that fine features of thin-cell spectra are not captured by Model A. This motivates extending the model to explicitly include the spatially varying vdW potential.

To do so, we now make the transition frequency spatially dependent: $\omega_{FF'} \rightarrow \omega_{FF'} + V(z)$. The atom-surface position-dependent shift of the $D1$ transition frequency is $V(z) = -C_3[1/z^3 + 1/(L - z)^3]$, where $C_3 = C_3[6P_{1/2}] - C_3[6S_{1/2}]$. In independently summing the potentials of each surface, we account only for the interaction of the atomic dipole with its image from the two surfaces. Image dipoles of image dipoles have contributions smaller than $\sim 3\%$ (Appendix C).

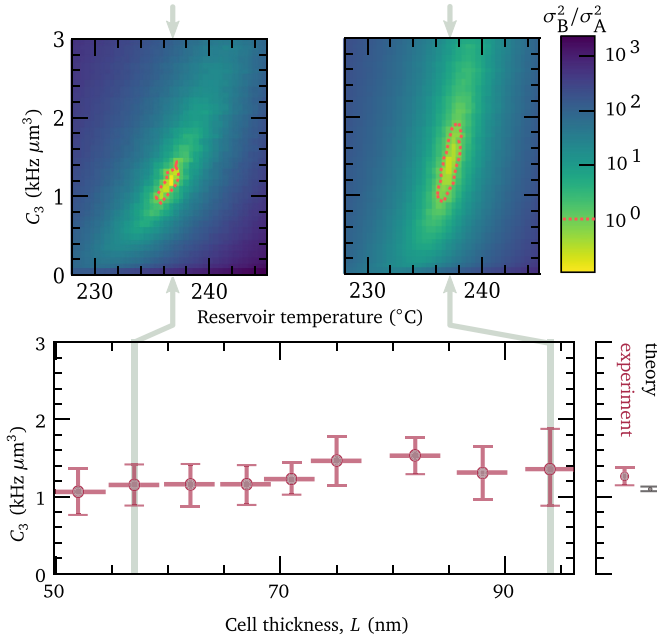


FIG. 4. Determination of the C_3 coefficient for the $D1$ line of Cs atoms close to the sapphire surface. Top insets: temperature- C_3 maps of the sum of squared residuals σ_B^2 for Model B, normalized by σ_A^2 for the best fit with Model A. The ratio for two cell thicknesses is indicated by vertical shaded bars on the main plot. The red dotted curve delineates the area where Model B is better than the best fit with Model A. Main plot: C_3 (circles) obtained by fitting Model B to the transmission spectra for different cell thickness. Error bars are systematic. The final value of C_3 , obtained as a weighted average, is in excellent agreement with the theoretical prediction (side scale).

Solving the Bloch equations leads to the solution for the atomic coherence field of the same form as in Eqs. (1) and (2), except that now

$$\Lambda_{\pm}(z) = \left\{ \frac{\Gamma_0 + \Gamma_{P0}}{2} - i(\omega - \omega_{FF'} - \Delta_{P0} \mp kv) + iC_3 \left[\frac{1}{2z^3} - \frac{1}{2z(L-z)^2} \right] \right\} z. \quad (5)$$

Here we set the collisional broadening Γ_{P0} to be the same as in the bulk, which is justified as we are far from polaritonic resonances of the crystal surface [40]. The first part of Eq. (5) describes the bulk [Eq. (3)], while the second line is due to the atom-surface vdW potential. By using Eq (5) in Eqs. (1) and (2), we include the *internal* atomic dynamics as the atoms move relative to the surface, thus experiencing a *time-varying level shift* due to the vdW interaction $V(z)$, to obtain the coherence field for each velocity class at location z . In previous works based on fluorescence measurement [30], the motion was not accounted for [31]. For details of the numerical integration, see Appendix A. We call this Model B.

The result of the fitting of the data for a thin cell with $L = 60$ nm is shown in Fig. 3. Model B has only two free parameters, the temperature and C_3 , as Γ_{P0} and Δ_{P0} are constrained to their bulk extracted values. Yet, it shows outstanding agreement compared to Model A that only phenomenologically accounts for atom-surface vdW interactions. In particular, the red-side asymmetry cannot be retrieved

without properly taking the vdW shift into account. We note that this asymmetry has also been observed using a cold-atomic cloud confined near a nanofiber [12]. The value for C_3 is extracted from fitting the spectra for each cell thickness L (Fig. 4, main panel). Thin cells yield a larger fraction of atoms close to the surface, where the vdW potential induces large level shifts, and allow tighter constraints on the fitted parameters. This is visible on the map represented in the top insets of Fig. 4, where the region that minimizes the sum of the squared residuals for Model B, σ_B^2 , is more tightly localized along the C_3 axis for thin cells. We also show more quantitatively the regime of parameters for which Model B is better than Model A. The error bars on C_3 (main panel of Fig. 4) are systematic and result from propagating errors on the cell thickness and the fitted bulk vapor parameters Γ_{P0} and Δ_{P0} (Appendix B). Assuming no dependence on L , the final value for C_3 is obtained as an average of the fitted values for different cell thicknesses weighted by their individual error bars [41]. We obtain $C_3 = 1.26 \pm 0.10$ kHz μm^3 , in good agreement (Fig. 4 side scale) with the theoretical value $C_3^{\text{th}} = 1.10 \pm 0.03$ kHz μm^3 (Appendix C) predicted from the Lifshitz theory of vdW interactions [42], based on the refractive index of sapphire [43] and the latest calculations of dipole matrix elements for low-lying cesium transitions [44,45].

V. CONCLUSION

In conclusion, we have demonstrated a method to measure the interaction between an atom and a surface. It relies on comparing the transmission of a laser beam through a wedged nanocell filled with an atomic vapor to a theoretical model including the atom-surface interaction, cavity effects, collisions with surfaces of the cell, and atomic motion. The wedged cell provides simultaneous access to the bulk vapor properties, tightly constraining theoretical parameters, and thin-cell regions with strong vdW interaction. We have illustrated the method with thermal cesium atoms confined within a sapphire cell and measured the $D1$ transition shift due to the cesium-sapphire interaction. Our model yields transmission predictions in excellent agreement with the experimental data. The measured C_3 coefficient is consistent with the nonresonant Lifshitz theory. Further improvements in precision are expected from adapting this work to fluorescence measurements, as a better signal-to-noise ratio leads to a better determination of the collisional properties as well as a reduction of statistical errors in extremely thin regions. Finally, this work opens the way to quantitative analysis of atom dynamics close to surfaces in new platforms [6,11,12], the search for predicted atom-surface repulsive potential [28] and bound states [46], and the examination of short-range [47] and long-range [48] limits of atom-surface potential, using thermal vapor spectroscopy.

The data and the code for the theoretical model are both available [50,51].

ACKNOWLEDGMENTS

We thank A. Laliotis and J. Keaveney for fruitful discussions. T.P. is financially supported by the DGA-DSTL

Fellowship No. 2015600028. N.Š. is financially supported by H2020 Marie Skłodowska-Curie Actions (Fellowship No. 786702). We also acknowledge financial support from EPSRC (Grant No. EP/R002061/1) and Durham University.

APPENDIX A: DERIVATION OF THE VAPOR-CELL TRANSMISSION

In this Appendix, we present a detailed derivation of the expression for the transmission through the atomic vapor slab, including the optical cavity effect due to the sapphire windows of the nanocell and the vdW atom-surface interaction. We start by deriving the expression of the polarization $P(z, \omega)$ of the ensemble of atoms and we subsequently compute the transmission through the nanocell. The derivation is done in the limit of an optically thin vapor.

1. Calculation of the vapor polarization P

We use a one-dimensional (1D) model for the propagation along the z axis of the field through the vapor. We decompose the linearly polarized, monochromatic field driving the atom inside the cavity formed by the sapphire plates,

$$E(z, t) = \frac{1}{2}[E(z)e^{-i\omega t} + E^*(z)e^{i\omega t}], \quad (\text{A1})$$

and the polarization of the atomic vapor,

$$P(z, t) = \frac{1}{2}[P(z)e^{-i\omega t} + P^*(z)e^{i\omega t}], \quad (\text{A2})$$

in their positive- and negative-frequency components. We first consider a given atomic transition between ground and excited states, with respective hyperfine states F and F' . The transition frequency is $\omega_{FF'}$, the total homogeneous linewidth Γ_t , and the dipole matrix element $d_{FF'}$ for the driven transition by the linearly polarized laser field. For this transition, we introduce the classical coherence field $\rho_{21}(z, t, v) = \langle \rho_{21}^{(i)}(t, v) \rangle_{\text{atoms}}$, where $\langle \cdot \rangle$ is the configuration average of the coherences $\rho_{21}^{(i)}$ of all atoms i located within the $(z, z + \delta z)$ slab and with velocities in the range $(v, v + \delta v)$, where $\delta z, \delta v \rightarrow 0$. The evolution of this field is given by the hydrodynamic equation

$$\begin{aligned} & \frac{\partial \rho_{21}(z, t, v)}{\partial t} \\ &= \underbrace{-i\omega_{FF'}\rho_{21}(z, t, v) + i\frac{d_{FF'}E(z, t)}{\hbar} - \frac{\Gamma_t}{2}\rho_{21}(z, t, v)}_{\text{Internal atom evolution (Bloch equations)}} \\ & \times \underbrace{-v\frac{\partial \rho_{21}(z, t, v)}{\partial z}}_{\text{atoms flying into and out from the slab at position } z}. \end{aligned} \quad (\text{A3})$$

The first part of the right-hand side of the equation is the standard Bloch equations for the evolution of the coherence under weak driving, when the population of the excited state can be neglected ($\rho_{22} \rightarrow 0$) [49]. In addition, since the field is defined as an average over many atoms at a given location z , it can also change due to atoms flying into and out of the vapor slab at position z . This is accounted for by the second part of the right-hand side of Eq. (A3), which appears owing to the fact that we consider the coherence *field* rather than the coherence of a given atom. It is valid assuming that the vapor

is homogeneous, i.e., the atom number density \mathcal{N} for a given velocity is the same everywhere in the vapor [$\partial \mathcal{N}(z, v)/\partial z = 0$]. This is a very good approximation as long as the kinetic energy of the atoms is much larger than the potential energy induced by the vdW interactions, i.e., for $z > (2C_3/k_B T)^{1/3} = 0.6$ nm. Using Eq. (A1) and the rotating wave approximation, we obtain the time-independent equation

$$v\frac{\partial \rho_{21}(z, v)}{\partial z} = -\left[\frac{\Gamma_t}{2} - i\Delta_{FF'}\right]\rho_{21}(z, v) + i\frac{d_{FF'}E(z)}{2\hbar}, \quad (\text{A4})$$

where $\Delta_{FF'} = \omega - \omega_{FF'}$ is the laser-frequency detuning from the atomic transition and Γ_t the total homogeneous linewidth. For the general driving field,

$$E(z) = E_+e^{ikz} + E_-e^{-ikz}, \quad (\text{A5})$$

consisting of the copropagating E_+ and counterpropagating E_- field along the z axis with $k = \omega/c$ the laser wave vector, we write the coherence as

$$\rho_{21}(z, v) = \rho_+(z, v)e^{ikz} + \rho_-(z, v)e^{-ikz}. \quad (\text{A6})$$

We thus obtain the following two equations from Eq. (A4):

$$v\frac{\partial \rho_+}{\partial z} = -[\Gamma_t/2 - i(\Delta_{FF'} - kv)]\rho_+ + i\frac{d_{FF'}E_+}{2\hbar}, \quad (\text{A7})$$

$$v\frac{\partial \rho_-}{\partial z} = -[\Gamma_t/2 - i(\Delta_{FF'} + kv)]\rho_- + i\frac{d_{FF'}E_-}{2\hbar}. \quad (\text{A8})$$

In the two expressions above, both Γ_t and $\omega_{FF'}$ may depends on z , for example due to the atom-surface interaction potential. Using the variation of constant method for differential equations, we find, for $v \neq 0$,

$$\begin{aligned} \rho_+(z, v) &= \rho_+(z_0, v)e^{-\Lambda_+/v} \\ &+ i\frac{d_{FF'}E_+}{2\hbar v} \int_{z_0}^z dz' \exp\left[\frac{\Lambda_+(z') - \Lambda_+(z)}{v}\right], \end{aligned} \quad (\text{A9})$$

$$\begin{aligned} \rho_-(z, v) &= \rho_-(z_0, v)e^{-\Lambda_-/v} \\ &+ i\frac{d_{FF'}E_-}{2\hbar v} \int_{z_0}^z dz' \exp\left[\frac{\Lambda_-(z') - \Lambda_-(z)}{v}\right], \end{aligned} \quad (\text{A10})$$

where the primitive

$$\Lambda_{\pm}(z) = \int^z \frac{\Gamma_t(u)}{2} - i[\Delta_{FF'}(u) \mp kv] du. \quad (\text{A11})$$

Assuming a loss of coherence resulting from the collisions of the atoms with the cell walls [35] (quenching collisions) leads to the boundary conditions $\rho_{\pm}(v > 0, z = 0) = \rho_{\pm}(v < 0, z = L) = 0$. Three cases can be distinguished:

(i) $v > 0$:

$$\rho_+(z, v > 0) = i\frac{d_{FF'}E_+}{2\hbar v} \int_0^z dz' \exp\left[\frac{\Lambda_+(z') - \Lambda_+(z)}{v}\right], \quad (\text{A12})$$

$$\rho_-(z, v > 0) = i\frac{d_{FF'}E_-}{2\hbar v} \int_0^z dz' \exp\left[\frac{\Lambda_-(z') - \Lambda_-(z)}{v}\right]; \quad (\text{A13})$$

(ii) $v < 0$:

$$\rho_+(z, v < 0) = -i \frac{d_{FF'} E_+}{2\hbar v} \int_z^L dz' \exp \left[\frac{\Lambda_+(z') - \Lambda_+(z)}{v} \right], \quad (\text{A14})$$

$$\rho_-(z, v < 0) = -i \frac{d_{FF'} E_-}{2\hbar v} \int_z^L dz' \exp \left[\frac{\Lambda_-(z') - \Lambda_-(z)}{v} \right]; \quad (\text{A15})$$

(iii) $v = 0$:

$$\rho_{\pm}(z, v = 0) = \frac{id_{FF'} E_{\pm}/2\hbar}{\Gamma_1/2 - i\Delta_{FF'}}. \quad (\text{A16})$$

Now, knowing the coherences in Eq. (A6), we calculate the polarization given by Eq. (A2) by integrating the total atomic dipole moment over the Maxwell-Boltzmann velocity distribution $M_b(v)$, and adding all relevant transitions $F \rightarrow F'$,

$$P(z, \omega) = \sum_{F, F'} \int_{-\infty}^{\infty} 2\mathcal{N}M_b(v) d_{FF'} [\rho_-(z, v, \omega) e^{-ikz} + \rho_+(z, v, \omega) e^{+ikz}] dv. \quad (\text{A17})$$

When the vdW potential is not taken into account, $\omega_{FF'}$ and Γ_1 are independent of z . In this case, Eq. (A17) gives analytical expressions that we derived in Ref. [32]. Here instead, we consider the atom-surface potential. As a consequence, a specific optical transition for an atom located at a distance z from the first surface is shifted as $\omega_{FF'}(z) = \omega_{FF'} - [C_3/z^3 + C_3/(L-z)^3]$. Far from any polaritonic resonances of the crystal surface, the linewidth may, however, be considered as independent of z and $\Gamma_1(z) = \Gamma_1$ [40]. We can then calculate the integrals of Eq. (A11),

$$\Lambda_{\pm} = \left\{ \frac{\Gamma_1}{2} - i \left[\Delta \mp kv - \frac{C_3}{2z^3} + \frac{C_3}{2z(L-z)^2} \right] \right\} z. \quad (\text{A18})$$

The expression now diverges for $z = 0$ and $z = L$. Besides, none of Eqs. (A12), (A13), (A15), and (A17) provide analytical solutions. These integrals are regularized by introducing a minimal cutoff distance $L_{\text{cut}} = 0.1$ nm from both surfaces. We have checked that it does not influence the results of the numerical computation.

2. Calculation of the driving and transmitted fields in the presence of the cavity

The cell walls are two interfaces for the incoming driving light E_0 (Fig. 5). The first sapphire-vapor interface is characterized by transmission $t_1 = 2n/(1+n)$ and reflection $r_1 = (n-1)/(1+n)$ amplitude coefficients, where $n = 1.76$ is the sapphire refractive index. The second vapor-sapphire interface coefficients are $t_2 = 2/(1+n)$ for the transmission and $r_2 = (1-n)/(1+n)$ for the reflection. Due to the low-finesse cavity nature of the cell, the driving field is also multiply reflected. The total driving field inside the cavity is therefore $E = E_+ e^{ikz} + E_- e^{-ikz}$, with

$$E_+ = E_0 \frac{t_1}{1 - r_2^2 e^{2ikL}}, \quad (\text{A19})$$

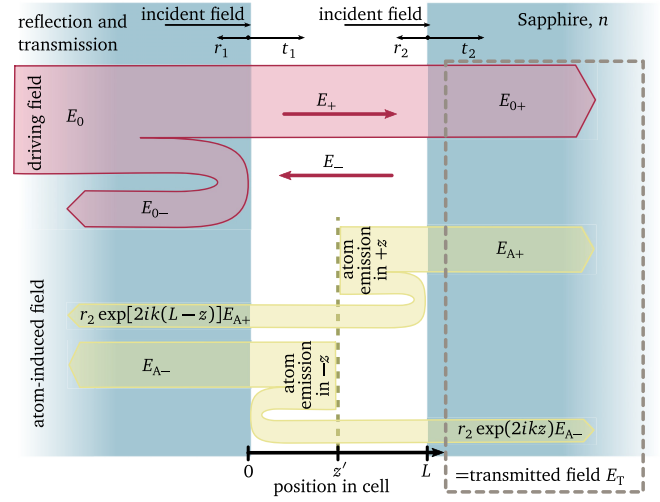


FIG. 5. Reflection and transmission of fields on sapphire-vapor and vapor-sapphire interfaces. The incident driving field E_0 is split by this interface into a transmitted field E_{0+} and a reflected field E_{0-} . Inside the low-finesse cavity formed by these two interfaces, the driving field gives rise to a field E_+ propagating along the z -axis direction, and a counterpropagating field E_- . The field emitted by the atoms *inside the cavity* in the forward direction after multiple reflections by the cavity results in the fields E_{A+} and $r_2 \exp[2ik(L-z)]E_{A+}$ propagating *outside the cavity* in the $+z$ and $-z$ directions, respectively. Similarly, the field emitted initially by the atoms in the $-z$ direction results in the fields E_{A-} and $r_2 \exp(2ikz)E_{A-}$ propagating *outside the cavity* in the $-z$ and $+z$ directions, respectively.

and

$$E_- = E_0 \frac{t_1 r_2 e^{2ikL}}{1 - r_2^2 e^{2ikL}}. \quad (\text{A20})$$

Here, $k = \omega/c$ is the field wave vector *in vacuum*, as we assume that the vapor is optically thin so as to neglect its index of refraction. The transmitted driving field is therefore

$$E_{0+} = E_0 \frac{t_1 t_2}{1 - r_2^2 e^{2ikL}}. \quad (\text{A21})$$

We now derive the field scattered by the polarization of the atomic vapor. The field emitted by the atoms *inside the cavity* along the z axis ($+z$ direction) experiences multiple reflections between the two sapphire windows (see Fig. 5), resulting in the fields E_{A+} and $r_2 \exp[2ik(L-z)]E_{A+}$ propagating *outside the cavity* in the $+z$ and $-z$ direction, respectively, where

$$E_{A+} = \frac{t_2}{1 - r_2^2 e^{2ikL}} \frac{ik}{2\epsilon_0} \int_0^L dz' P(z', \omega) e^{ik(z-z')}. \quad (\text{A22})$$

Similarly, the field originally emitted by the atoms *inside the cavity* in the $-z$ direction, after multiple reflections by the cell windows, results in fields E_{A-} and $r_2 \exp(2ikz)E_{A-}$ propagating *outside the cavity* in the $-z$ and $+z$ directions, respectively, where

$$E_{A-} = \frac{t_2}{1 - r_2^2 e^{2ikL}} \frac{ik}{2\epsilon_0} \int_0^L dz' P(z', \omega) e^{-ik(z-z')}. \quad (\text{A23})$$

The transmitted field along the z axis is then given by the sum of the driving field and atom-induced field contributions,

$$E_{T+} = E_{0+} + E_{A+} + r_2 \exp(2ikz)E_{A-}. \quad (\text{A24})$$

The relative transmission is thus $T = |E_T/E_{0+}|^2$.

Note. We highlight one nanocell peculiarity in comparison to more standard, thick cells, regarding the directionality of emitted light. Using the expression for polarization given by Eq. (A17) in Eq. (A22) for emission along the laser beam, we obtain

$$E_{A+} \propto \int_0^L \rho_+ dz' + \int_0^L \rho_- e^{-2ikz'} dz'. \quad (\text{A25})$$

For thick cells ($L \gg \lambda$) and slowly varying coherence fields ρ_+ and ρ_- , we note that the rapid integrand sign change in the second term prevents contribution of ρ_- to E_{A+} . We obtain that emission in the $z+$ direction is then dominated by the ρ_+ part of the coherence field. However, for nanocells $L \ll \lambda$, the exponential factor is practically constant over the length of the cell, and we see that ρ_- also contributes to the emission in the $z+$ direction. This is expected if one keeps in mind that large atomic ensembles can emit light in a given direction thanks to the interference [given by Eq. (A22)] from phase grating (cf. Bragg grating) imprinted by the driving laser beam into the spatial variation of the coherence phase. However, cells $L \ll \lambda$ are not thick enough to contain a single period λ of this phase variation (Bragg grating), and emission integration in Eq. (A22) will not single out the contribution of ρ_+ to polarization [Eq. (A17)]. Instead, ρ_- will contribute to emission in the forward direction too. In particular, note that this is not the consequence of reflection of the light emitted along $z-$ on the interface. Indeed, the effect would exist even in the absence of cavity-induced reflections. This effect can also be seen as a consequence of constraint on the space-bandwidth product of the Fourier transform in space, which for small total distances cannot distinguish between the $+k$ and $-k$ components (cf. Heisenberg relations), giving a reduction of the phase-matching constraint for thin cells.

APPENDIX B: ESTIMATION OF THE ERROR BARS ON THE EXTRACTED C_3 VALUE

In this Appendix, we explain how we have assigned the error bars for the C_3 coefficients extracted from the transmission spectra corresponding to various thicknesses presented in Fig. 4 of the main text. We subsequently derive the final value and uncertainty for the atom-surface coefficient.

To extract the transmission in intensity from the raw data, we need to divide the measured transmitted intensity by the intensity far from the atomic resonance. In normalizing the data, an issue arises due to a residual variation of the intensity not corrected by the stabilization of the laser power during the scan across the atomic resonances. This residual variation may distort the line shape and introduce unphysical shifts. Our normalization procedures therefore account for this nearly linear intensity variation. We have checked that a small variation of the residual slope of the intensity variation does not significantly influence the fitted C_3 value (of the order of a few percent). We then checked that the statistical

TABLE I. Dominant contributions to the cesium-sapphire van der Waals constant C_3 for $6S_{1/2}$ and $6P_{1/2}$ states, with listed references for dipole matrix elements μ^{ab} .

Hyperfine transition	Contribution to C_3^a (kHz μm^3)	Reference
$6S_{1/2} \leftrightarrow 6P_{1/2}$	0.42	[44]
$6S_{1/2} \leftrightarrow 6P_{3/2}$	0.83	[44]
$6S_{1/2} \leftrightarrow 7P_{3/2}$	0.01	[44]
Total $C_3^{6S_{1/2}} =$	1.258(2)	
$6P_{1/2} \leftrightarrow 6S_{1/2}$	0.42	[44]
$6P_{1/2} \leftrightarrow 7S_{1/2}$	0.37	[44]
$6P_{1/2} \leftrightarrow 8S_{1/2}$	0.02	[45]
$6P_{1/2} \leftrightarrow 5D_{3/2}$	1.01	[44]
$6P_{1/2} \leftrightarrow 6D_{3/2}$	0.37	[44]
$6P_{1/2} \leftrightarrow 7D_{3/2}$	0.09	[44]
$6P_{1/2} \leftrightarrow 8D_{3/2}$	0.04	[45]
$6P_{1/2} \leftrightarrow 9D_{3/2}$	0.02	[45]
$6P_{1/2} \leftrightarrow 10D_{3/2}$	0.01	[45]
Total $C_3^{6P_{1/2}} =$	2.36(3)	

repetition of the measurements does not modify the extracted C_3 value.

As explained in the main text, in order to extract the C_3 coefficient, we fix the thickness measured with an uncertainty of 5 nm. Collisional linewidth and shift are also fixed to their bulk values Δ_{P0} and Γ_{P0} measured at large cell thicknesses. These values are the average of the shifts Δ_P and broadenings Γ_P obtained for thicknesses $L \geq 175$ nm, and the error bar on these parameters is the standard deviation of this ensemble of values. In order to assign an error bar to the C_3 coefficient, we perform an error propagation in the following way: we vary within their error intervals Δ_P and Γ_P and L and repeat the fitting procedure to find the C_3 that minimizes the sum of the squared residuals. We thus obtain the systematic error on C_3 associated to the uncertainty in the determination of Δ_{P0} and Γ_{P0} . For each cell thickness L , we then assign an error bar that encompasses all the C_3 values obtained in this way.

When applying this procedure, we find that the extracted C_3 is insensitive to the value of Γ_{P0} . On the contrary, it is very sensitive to the values of Δ_{P0} and L , which are by far the main contributors to the uncertainty of C_3 . The error bars assigned for each thickness in Fig. 4 of the main text correspond to the variation of C_3 by changing Δ_{P0} within ± 20 MHz range and L within ± 2.5 nm. For each thickness, the error bar associated to C_3 is the quadratic sum of the error due to Δ_{P0} and L .

In order to give a final value for the extracted C_3 , we make the final assumption that it does not vary with the cell thickness. This approximation supposes that retardation effects would not lead to an effective dependence of C_3 with L . The final value of the cesium-sapphire C_3 coefficient is then assigned, together with its error bar, as an average weighted by the individual points of the error bars. We find

$$C_3 = 1.26 \pm 0.10 \text{ kHz } \mu\text{m}^3. \quad (\text{B1})$$

APPENDIX C: THEORETICAL CALCULATION OF C_3^{th}

The level shift $V_a(z)$ experienced by an atom in a state $|a\rangle$, placed in front of a dielectric surface with refractive index

$n(\omega)$, is given by (see, for example, [36])

$$V_a(z) = -\frac{1}{4\pi\epsilon_0} \sum_{\text{states } |b\rangle} \frac{n(\omega_{ab})^2 - 1}{n(\omega_{ab})^2 + 1} \frac{|\mu_x^{ab}|^2 + |\mu_y^{ab}|^2 + 2|\mu_z^{ab}|^2}{16z^3} \\ \equiv -\frac{C_3^a}{z^3}. \quad (\text{C1})$$

The prefactor depending on the refractive index $n(\omega_{ab})$ at the frequency ω_{ab} of an atomic transition $|a\rangle \rightarrow |b\rangle$ accounts for the strength of the image dipole formed inside the dielectric. It would be equal to 1 for a perfectly reflective surface. The sum is over all states $|b\rangle$ that are dipole coupled to $|a\rangle$, and $\mu_{x\dots z}^{ab}$ are the dipole matrix elements corresponding to the dipole orientations along the x , y , and z axis, respectively. Knowing the refractive index of the surface for a range of frequencies and the dipole matrix elements of the corresponding

transitions allows one to calculate the energy shift of a given state due to van der Waals interaction, as given in Table I. In this table, the dipole matrix elements are theoretically calculated values from Ref. [44] and the alkali Rydberg calculator (ARC) PYTHON package [45]. The refractive index of ordinary sapphire is calculated from the data in Ref. [43]. Using the values in Table I, we finally obtain the theoretical van der Waals coefficient for the shift of the $6S_{1/2} \rightarrow 6P_{1/2}$ transition,

$$C_3^{\text{th}} = C_3[6P_{1/2}] - C_3[6S_{1/2}] = 1.10 \pm 0.03 \text{ kHz } \mu\text{m}^3. \quad (\text{C2})$$

The expression (C1) used for $V_a(z)$ accounts only for the interaction of a dipole with its image in the sapphire. The interaction of the dipole image with its dipole image, and higher, is neglected. The full potential would have the form [19]

$$V_a^{\text{tot}}(z) = -\frac{1}{4\pi\epsilon_0} \sum_{\text{states } |b\rangle} \left\{ \frac{|\mu_x^{ab}|^2 + |\mu_y^{ab}|^2 + 2|\mu_z^{ab}|^2}{16} \sum_{m=0}^{\infty} \left[\frac{1}{(z+mL)^3} + \frac{1}{(L-z+mL)^3} \right] \delta(\omega_{ab})^{2m+1} \right. \\ \left. - \frac{|\mu_x^{ab}|^2 + |\mu_y^{ab}|^2 - 2|\mu_z^{ab}|^2}{16} \sum_{m=1}^{\infty} \frac{2}{(mL)^3} \delta(\omega_{ab})^{2m} \right\}, \quad (\text{C3})$$

where $\delta(\omega_{ab}) = [n(\omega_{ab})^2 - 1]/[n(\omega_{ab})^2 + 1]$ is a factor depending on the material, and where the first and second line correspond, respectively, to odd and even reflections. Due to spherical symmetry, $|\mu_x|^2 = |\mu_y|^2 = |\mu_z|^2$ and the second term vanishes. For the atoms in the middle of the cell, $z = L/2$ and the contribution of the $m = 1$ term will already be $1/3^3$ smaller (closer to the surfaces, the suppression will be

even stronger) due to the larger distance between the atoms and their image. The extra factor $\delta^2 \approx (0.5)^2$ leads to further suppression, giving a total contribution of the order of $\sim 1\%$ compared to the $m = 0$ term taken into account in the potential $V(z)$ used in the main text. Higher-order reflections are even more suppressed. Thus the potential $V(z)$ used in the main text is a good approximation of the V^{tot} to within $\sim 3\%$.

-
- [1] D. E. Chang, J. S. Douglas, A. González-Tudela, C. L. Hung, and H. J. Kimble, *Rev. Mod. Phys.* **90**, 31002 (2018).
- [2] P. Lodahl, S. Mahmoodian, S. Stobbe, A. Rauschenbeutel, P. Schneeweiss, J. Volz, H. Pichler, and P. Zoller, *Nature (London)* **541**, 473 (2017).
- [3] C. Stehle, C. Zimmermann, and S. Slama, *Nat. Phys.* **10**, 937 (2014).
- [4] R. Mitsch, C. Sayrin, B. Albrecht, P. Schneeweiss, and A. Rauschenbeutel, *Nat. Commun.* **5**, 5713 (2014).
- [5] D. Chang, A. Sørensen, E. Demler, and M. Lukin, *Nat. Phys.* **3**, 807 (2007).
- [6] D. J. Alton, N. P. Stern, T. Aoki, H. Lee, E. Ostby, K. J. Vahala, and H. J. Kimble, *Nat. Phys.* **7**, 159 (2010).
- [7] D. E. Chang, V. Vuletić, and M. D. Lukin, *Nat. Photon.* **8**, 685 (2014).
- [8] F. Le Kien, V. I. Balykin, and K. Hakuta, *Phys. Rev. A* **70**, 063403 (2004).
- [9] G. Sagué, E. Vetsch, W. Alt, D. Meschede, and A. Rauschenbeutel, *Phys. Rev. Lett.* **99**, 163602 (2007).
- [10] E. Vetsch, D. Reitz, G. Sagué, R. Schmidt, S. T. Dawkins, and A. Rauschenbeutel, *Phys. Rev. Lett.* **104**, 203603 (2010).
- [11] K. Deasy, C. F. Phelan, V. G. Truong, S. Nic Chormaic, and M. Daly, *New J. Phys.* **16**, 053052 (2014).
- [12] B. D. Patterson, P. Solano, P. S. Julienne, L. A. Orozco, and S. L. Rolston, *Phys. Rev. A* **97**, 032509 (2018).
- [13] D. Sarkisyan, D. Bloch, A. Papoyan, and M. Ducloy, *Opt. Commun.* **200**, 201 (2001).
- [14] T. Peyrot, C. Beurthe, S. Coumar, M. Roullia, K. Perronet, P. Bonnay, C. S. Adams, A. Browaeys, and Y. R. P. Sortais, *Opt. Lett.* **44**, 1940 (2019).
- [15] R. Ritter, N. Gruhler, H. Dobbertin, H. Kübler, S. Scheel, W. Pernice, T. Pfau, and R. Löw, *Phys. Rev. X* **8**, 021032 (2018).
- [16] S. Knappe, P. D. D. Schwindt, V. Shah, L. Hollberg, J. Kitching, L. Liew, and J. Moreland, *Opt. Express* **13**, 1249 (2005).
- [17] R. T. Wakai, G. S. Smetana, T. G. Walker, M. Kauer, and R. Wyllie, *Phys. Med. Biol.* **57**, 2619 (2012).
- [18] C. G. Wade, N. Šibalić, N. R. de Melo, J. M. Kondo, C. S. Adams, and K. J. Weatherill, *Nat. Photon.* **11**, 40 (2017).
- [19] E. A. Hinds, in *Advances in Atomic, Molecular, and Optical Physics*, edited by D. Bates and B. Bederson, Vol. 28 (Academic, Cambridge, MA, 1990), p. 237.
- [20] At larger distances, interaction potential retardation effects have to be taken into account, resulting in Casimir-Polder potential $\propto z^{-4}$. See, e.g., review [19].
- [21] A. Landragin, J. Y. Courtois, G. Labeyrie, N. Vansteenkiste, C. I. Westbrook, and A. Aspect, *Phys. Rev. Lett.* **77**, 1464 (1996).

- [22] R. E. Grisenti, W. Schöllkopf, J. P. Toennies, G. C. Hegerfeldt, and T. Köhler, *Phys. Rev. Lett.* **83**, 1755 (1999).
- [23] F. Shimizu, *Phys. Rev. Lett.* **86**, 987 (2001).
- [24] A. K. Mohapatra and C. S. Unnikrishnan, *Europhys. Lett.* **73**, 839 (2006).
- [25] M. Fichet, G. Dutier, A. Yarovitsky, P. Todorov, I. Hamdi, I. Maurin, S. Saltiel, D. Sarkisyan, M. P. Gorza, D. Bloch, and M. Ducloy, *Europhys. Lett.* **77**, 54001 (2007).
- [26] V. Sandoghdar, C. I. Sukeik, E. A. Hinds, and S. Haroche, *Phys. Rev. Lett.* **68**, 3432 (1992).
- [27] M. Oria, M. Chevrollier, D. Bloch, M. Fichet, and M. Ducloy, *Europhys. Lett.* **14**, 527 (1991).
- [28] H. Failache, S. Saltiel, M. Fichet, D. Bloch, and M. Ducloy, *Phys. Rev. Lett.* **83**, 5467 (1999).
- [29] A. Sargsyan, A. Papoyan, I. G. Hughes, C. S. Adams, and D. Sarkisyan, *Opt. Lett.* **42**, 1476 (2017).
- [30] K. A. Whittaker, J. Keaveney, I. G. Hughes, A. Sargsyan, D. Sarkisyan, and C. S. Adams, *Phys. Rev. Lett.* **112**, 253201 (2014).
- [31] D. Bloch, *Phys. Rev. Lett.* **114**, 049301 (2015).
- [32] T. Peyrot, Y. R. P. Sortais, J. J. Greffet, A. Browaeys, A. Sargsyan, J. Keaveney, I. G. Hughes, and C. S. Adams, *Phys. Rev. Lett.* **122**, 113401 (2019).
- [33] M. A. Zentile, J. Keaveney, L. Weller, D. J. Whiting, C. S. Adams, and I. G. Hughes, *Comput. Phys. Commun.* **189**, 162 (2015).
- [34] T. Peyrot, Y. R. P. Sortais, A. Browaeys, A. Sargsyan, D. Sarkisyan, J. Keaveney, I. G. Hughes, and C. S. Adams, *Phys. Rev. Lett.* **120**, 243401 (2018).
- [35] M. F. H. Schuurmans, *Le J. Phys.* **37**, 469 (1976).
- [36] M. Fichet, F. Schuller, D. Bloch, and M. Ducloy, *Phys. Rev. A* **51**, 1553 (1995).
- [37] D. Bloch and M. Ducloy, in *Advances in Atomic, Molecular, and Optical Physics*, edited by B. Bederson and H. Walther, Vol. 50 (Academic, Cambridge, MA, 2005), p. 91.
- [38] G. Dutier, S. Saltiel, D. Bloch, and M. Ducloy, *J. Opt. Soc. Am. B* **20**, 793 (2003).
- [39] V. Vuletić, V. A. Sautenkov, C. Zimmermann, and T. W. Hänsch, *Opt. Commun.* **99**, 185 (1993).
- [40] H. Failache, S. Saltiel, A. Fischer, D. Bloch, and M. Ducloy, *Phys. Rev. Lett.* **88**, 243603 (2002).
- [41] I. G. Hughes and T. P. A. Hase, *Measurements and their Uncertainties* (Oxford University Press, Oxford, 2010).
- [42] E. Lifshitz, *Exper. Theoret. Phys. USSR* **29**, 94 (1956) [*Sov. Phys. JETP* **2**, 73 (1956)].
- [43] *Handbook of Optical Materials*, edited by M. J. Weber (CRC Press, Boca Raton, FL, 2003).
- [44] M. S. Safronova, U. I. Safronova, and C. W. Clark, *Phys. Rev. A* **94**, 012505 (2016).
- [45] N. Šibalić, J. D. Pritchard, C. S. Adams, and K. J. Weatherill, *Comput. Phys. Commun.* **220**, 319 (2017).
- [46] E. G. Lima, M. Chevrollier, O. Di Lorenzo, P. C. Segundo, and M. Oriá, *Phys. Rev. A* **62**, 013410 (2000).
- [47] M. C. Vargas and W. L. Mochán, *Surf. Sci.* **409**, 130 (1998).
- [48] J. C. deAquino Carvalho, P. Pedri, M. Ducloy, and A. Laliotis, *Phys. Rev. A* **97**, 023806 (2018).
- [49] G. Grynberg, A. Aspect, and C. Fabre, *Introduction to Quantum Optics: From the Semi-classical Approach to Quantized Light* (Cambridge University Press, Cambridge, 2010).
- [50] T. Peyrot, N. Šibalić, Y. R. P. Sortais, A. Browaeys, A. Sargsyan, D. Sarkisyan, I. G. Hughes, and C. S. Adams, Research data for “Measurement of the atom-surface van der Waals interaction by transmission spectroscopy in a wedged nano-cell,” (Version 1.0.0.) Zenodo, <http://doi.org/10.5281/zenodo.2653100> (2019).
- [51] T. Peyrot, N. Šibalić, Y. R. P. Sortais, A. Browaeys, A. Sargsyan, D. Sarkisyan, I. G. Hughes, and C. S. Adams, Thermal-vapours/TAS-Transmission-Atom-Surface: TAS-Transmission-Atom-Surface release ver 0.0.3 (Version 0.0.3). Zenodo, <https://doi.org/10.5281/zenodo.2653126> (2019).